

# CommUNext: Deep Learning-Based Cross-Band and Multi-Directional Signal Prediction

Chi-Jui Sung, Fan-Hao Lin, Tzu-Hao Huang, Chu-Hsiang Huang, *Member, IEEE*, Hui Chen, *Member, IEEE*, Chao-Kai Wen, *Fellow, IEEE*, Henk Wymeersch, *Fellow, IEEE*

**Abstract**—Sixth-generation (6G) networks are envisioned to achieve full-band cognition by jointly utilizing spectrum resources from Frequency Range 1 (FR1) to Frequency Range 3 (FR3, 7–24 GHz). Realizing this vision faces two challenges. First, physics-based ray tracing (RT), the standard tool for network planning and coverage modeling, becomes computationally prohibitive for multi-band and multi-directional analysis over large areas. Second, current 5G systems rely on inter-frequency measurement gaps for carrier aggregation and beam management, which reduce throughput, increase latency, and scale poorly as bands and beams proliferate. These limitations motivate a data-driven approach to infer high-frequency characteristics from low-frequency observations. This work proposes CommUNext, a unified deep learning framework for cross-band, multi-directional signal strength (SS) prediction. The framework leverages low-frequency coverage data and crowd-aided partial measurements at the target band to generate high-fidelity FR3 predictions. Two complementary architectures are introduced: Full CommUNext, which substitutes costly RT simulations for large-scale offline modeling, and Partial CommUNext, which reconstructs incomplete low-frequency maps to mitigate measurement gaps in real-time operation. Experimental results show that CommUNext delivers accurate and robust high-frequency SS prediction even with sparse supervision, substantially reducing both simulation and measurement overhead.

**Index Terms**—6G networks, full-band cognition, cross-band prediction, multi-directional signal strength, deep learning, measurement gap reduction, ray tracing.

## I. INTRODUCTION

SIXTH-generation (6G) networks aim to integrate the full spectrum from Frequency Range 1 (FR1) to Frequency Range 3 (FR3), including the 7–24 GHz upper mid band [1], into a unified spectrum resource pool to support the six IMT-2030 usage scenarios [2]. Achieving this vision requires *full-band cognition*, which is the capability to sense and predict channel conditions across frequencies, beam directions, spatial locations, and time while minimizing active probing and

control overhead. Such cognition is essential for cross-band resource optimization, carrier aggregation (CA), and beam management in large-scale and dynamic deployments.

In the early stage of 6G network design, physics-based *ray tracing* (RT) serves as a vital tool for site planning, coverage evaluation, and link-budget analysis. RT simulations account for material properties, reflections, diffractions, and scattering to generate frequency-specific and direction-aware coverage maps. However, each simulation run typically produces only a single-band, single-beam output (e.g., Sionna [3] and Remcom Wireless InSite [4]). Extending RT to multi-band and multi-directional analyses over large urban areas drastically increases computational complexity and memory usage, often requiring hours or even days per region.<sup>1</sup> Although RT is primarily designed for offline coverage modeling rather than real-time operation, its extensive computational cost still poses a significant efficiency bottleneck even for offline analyses.

For real-time operation, current 5G New Radio (NR) systems rely on inter-frequency *measurement gaps* to discover carriers for CA, execute inter-band handovers, and perform beam management. During each gap, user equipment (UE) suspends reception on the serving link to probe another frequency (e.g., every 20/40/80 ms with a multi-slot gap) [5], [6]. While this mechanism is workable in existing systems, it reduces throughput, increases latency and power consumption, and scales poorly as 6G extends to full spectrum with finer beam codebooks. The cumulative cost of frequent multi-band probing renders gap-based coordination unsustainable.

These offline and operational challenges share a common origin in the evolving 6G spectrum landscape. In future deployments, the FR3 spectrum is expected to be co-located with existing FR1 macro sites, enabling infrastructure reuse and maintaining consistent spatial correlation [7], [8]. This co-location implies that low-frequency telemetry (e.g., 3.5 GHz), which is abundant and stable, can serve as a spatial proxy for higher-frequency environments. However, such low-frequency data may not always be complete in real operations, as user reports can be sparse, delayed, or unevenly distributed across regions. In addition, sparse high-band samples may be available rather than completely absent. These observations motivate a data-driven approach that utilizes rich but occasionally incomplete low-band data, together with sparse high-band samples, to predict multi-directional signal strength (SS) maps and enable scalable full-band cognition with reduced re-

Chi-Jui Sung, Fan-Hao Lin, and Chao-Kai Wen are with the Institute of Communications Engineering, National Sun Yat-sen University, Kaohsiung 80424, Taiwan (e-mail: johnnysung28@gmail.com; 22135lin@gmail.com; chaokai.wen@mail.nsysu.edu.tw).

Tzu-Hao Huang is with the Institute of Electrical Control Engineering, National Yang Ming Chiao Tung University, Hsinchu 300, Taiwan (e-mail: peter94135@gmail.com).

Chu-Hsiang Huang is with the Department of Electrical Engineering, National Taiwan University, Taipei 10617, Taiwan (e-mail: chuh-sianh@ntu.edu.tw).

Hui Chen and Henk Wymeersch are with the Department of Electrical Engineering, Chalmers University of Technology, 41296 Gothenburg, Sweden (emails: hui.chen@chalmers.se; henkw@chalmers.se).

This work was supported in part by the National Science and Technology Council of Taiwan under grant NSTC 114-2221-E-110-031-MY3 and the SNS JU project 6G-DISAC under the EU's Horizon Europe research and innovation programme under Grant Agreement No 101139130.

<sup>1</sup>For example, generating 133,956 received signal strength maps using Sionna, as in this work, requires approximately one month on a personal computer equipped with an RTX 2080 Ti GPU.

liance on both computationally intensive RT and measurement campaigns.

Building on this intuition, we propose **CommUNext**, a deep learning-based framework for *cross-band* and *multi-directional* signal prediction. The framework comprises two complementary architectures tailored to different data availability regimes. When a complete 3.5 GHz SS coverage map is available, **Full CommUNext** leverages it as a strong reference to predict high-band SS maps, addressing the limitations of RT-based offline modeling. When the low-frequency data are partially observed, such as when cloud-aggregated measurements are sparse or regionally missing, **Partial CommUNext** reconstructs the missing low-frequency map and transfers latent cross-band knowledge to enhance high-band prediction, thereby mitigating the impact of measurement gaps in live operation. In both cases, the framework integrates crowd-aided context by aggregating geo-aligned user reports that may include partial (opportunistic) measurements at the target band within the relevant time period, capturing dynamic blockage and environmental variations.

The main contributions of this work are summarized as follows:

- **Proposed a unified data-driven framework** that predicts *high-frequency, multi-directional* SS maps from low-frequency (3.5 GHz) coverage data and sparse high-frequency samples. The framework enables cross-band and multi-directional inference under both complete and incomplete reference-band conditions, thereby significantly reducing dependence on computationally intensive RT and measurement campaigns.
- **Designed two complementary network architectures, Full CommUNext and Partial CommUNext**, to realize this framework. The former leverages complete 3.5 GHz coverage maps as strong priors for cross-band prediction, while the latter reconstructs missing low-frequency information and transfers latent knowledge directly to enhance prediction under sparse supervision. **Partial CommUNext** achieves higher computational efficiency than naively passing the reconstructed 3.5 GHz coverage maps again to **Full CommUNext**.
- **Conducted extensive evaluations** using RT-based datasets to validate the proposed framework under various input prior conditions. The evaluations and analyses provide insights into which input priors are most relevant to cross-band prediction.

The remainder of this paper is organized as follows. Section II reviews related works; Section III describes data generation and preprocessing; Section IV details the data-driven framework and **CommUNext**; Section V presents experimental results; and Section VI concludes.

## II. RELATED WORKS

Traditional path-loss estimation relies on deterministic RT, which models reflection, diffraction, and scattering. While accurate in static environments, these methods are computationally expensive and unsuitable for large-scale or real-time tasks. Deep learning-based frameworks [9]–[11] address

this issue by offering fast and scalable inference with high accuracy. Early contributions include [12]–[14], and a survey is provided in [15]. These works collectively establish deep learning as a practical alternative to purely physics-based methods for radio propagation modeling.

Various architectures have been explored for radio map prediction. U-Net and its variants dominate early designs due to their strong spatial reconstruction capability [9], [13]. Attention U-Nets improve spatial feature weighting, enabling joint throughput and link-quality prediction [16]. Beyond CNNs, GNN-based methods capture irregular spatial-spectral relations [17], while GAN-based approaches (e.g., [18]) refine predictions through adversarial and task-driven learning. These diverse architectures highlight the importance of inductive biases in capturing propagation characteristics across heterogeneous environments.

Recent studies have further extended these methods toward cross-band prediction. HORCRUX focuses on frequency-division duplex systems by predicting downlink channels from uplink observations, emphasizing cross-environment generalization and scalability [19]. This task is link-level and relies on per-link uplink measurements, whereas our setting targets region-level, multi-directional SS maps driven by low-frequency coverage and sparse high-band samples. Another line of work integrates simulation and digital-twin modeling. RadioTwin combines material property modeling with RT engines to enable cross-band channel prediction [20]. While this approach embeds geometry and materials explicitly, it requires high-fidelity modeling and incurs substantial simulation cost. In contrast, our framework adopts a data-driven paradigm that leverages low-frequency maps and sparse high-band samples to reduce dependence on heavy RT and large-scale field surveys.

A complementary direction estimates system-level metrics. Geo2ComMap predicts higher-layer communication metrics such as throughput, Channel Quality Indicator (CQI), and Rank Indicator (RI), providing region-level performance maps [16]. Transformer-based methods further exploit historical multi-band measurements to forecast achievable rates over time [21]. These works operate at the service or system layer and primarily leverage performance indicators or temporal sequences, whereas our framework focuses on physical-layer SS maps with explicit multi-directional structure and cross-band transfer.

Datasets have also driven progress in this field. DeepMIMO [22] provides standardized mmWave MIMO data, while RadioMapSeer [23] supplies urban path-loss layers. The Indoor Radio Map Dataset [24] introduces large-scale benchmarks with sparse supervision, and [16] adds datasets covering throughput, CQI, and RI. These datasets reflect the growing demand for multi-band, multi-metric benchmarks that bridge physical- and system-level perspectives.

## III. DATA GENERATION AND PREPROCESSING

This section describes the data generation and preprocessing pipeline employed in this work. The process encompasses the acquisition of geographical information, simulation methodology, parameter configuration, and the preparation of both input



Figure 1. Automated data generation toolchain integrating OSM, Blender, and Sionna.

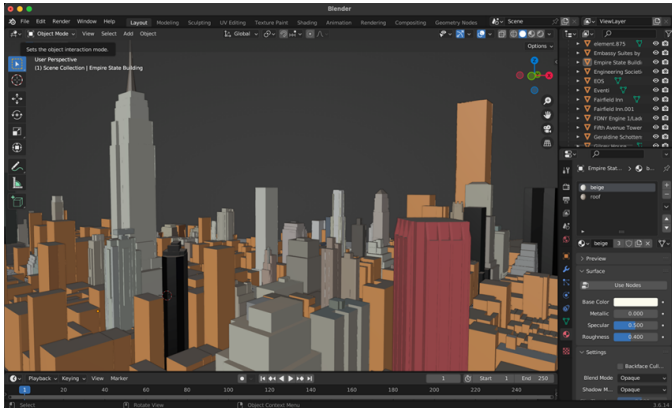


Figure 2. Example of importing OSM building data into Blender.

features and ground-truth labels for the data-driven neural network described in Section IV.

#### A. Automated Data Generation Toolchain

To emulate multi-directional and multi-band propagation, we developed an automated toolchain inspired by Geo2SigMap [13]. The framework integrates geographic information retrieval, 3D building modeling, and RT simulation, enabling the construction of realistic wireless datasets from real urban environments. The overall workflow is shown in Fig. 1 and involves three open-source components: OpenStreetMap (OSM), Blender, and NVIDIA Sionna.

1) *OSM and Blender*: Geographic data were obtained from OSM for the New York City metropolitan area covering  $[40.477399, 40.917577]$  latitude and  $[-74.259090, -73.700272]$  longitude. The area was partitioned into  $1\text{ km} \times 1\text{ km}$  blocks, and those with more than 20% building coverage were retained. Using the `bl_osc` plugin, building footprints were imported into Blender, converted into 3D meshes, and assigned material properties according to [25]. Each block produced (i) a building height map, (ii) Mitsuba-compatible 3D scene files, and (iii) metadata including boundaries, coverage ratio, and a Universally Unique Identifier (UUID). Fig. 2 illustrates an example of OSM data imported into Blender.

2) *NVIDIA Sionna*: The 3D scenes were simulated using the *NVIDIA Sionna Neural Radio Framework* [3], a GPU-accelerated library with differentiable RT [26], [27]. Sionna models reflection, diffraction, and scattering, and outputs path gain, received signal strength (RSS), and channel impulse responses. In this work, it was configured to:

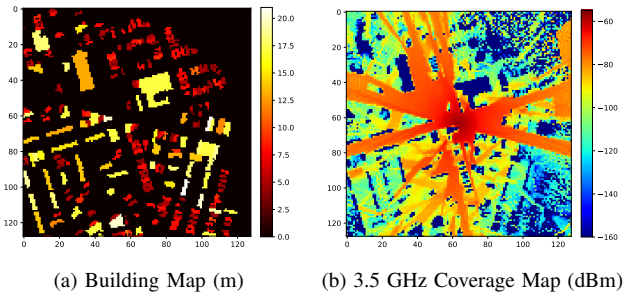


Figure 3. Example of (a) a building map  $\mathbf{B}$  and (b) the corresponding 3.5 GHz coverage map  $\mathbf{S}_c$ .

- Perform multi-band simulations at 3.5 and 7 GHz with user-specified transmitters, antenna patterns, and beam orientations.
- Generate omnidirectional coverage maps and eight-direction SS maps as supervised training labels.

#### B. Data Generation

To create datasets for model training, we combined OSM-derived building maps with NVIDIA Sionna RT simulations at 3.5 and 7 GHz. The workflow produces three key outputs: (i) building height maps  $\mathbf{B}$ , (ii) 3.5 GHz coverage maps  $\mathbf{S}_c$ , and (iii) eight-direction 7 GHz SS maps  $\{\mathbf{S}_{d1}, \mathbf{S}_{d2}, \dots, \mathbf{S}_{d8}\}$ , all aligned at a unified resolution of  $128 \times 128$  pixels.

1) *Building Maps*: For each  $1\text{ km} \times 1\text{ km}$  block in the New York City area, building footprints from OSM were converted into 3D meshes in Blender. A building height map of  $1000 \times 1000$  pixels was generated and cropped into four  $512 \times 512$  patches centered at the base station transmitter (Tx) positions. Each patch was then downsampled to  $128 \times 128$  to match the resolution of the signal coverage maps, as illustrated in Fig. 3(a).

2) *3.5 GHz Coverage Maps*: Using Sionna's differentiable ray tracer, 3.5 GHz propagation was simulated with isotropic Tx antennas located at the center of each building map. The simulator accounted for line-of-sight (LoS) paths, reflections, and diffractions, producing RSS values in dBm on a  $128 \times 128$  grid, as shown in Fig. 3(b). Table I summarizes the key simulation parameters, including carrier frequency, antenna height, and spatial resolution.

3) *7 GHz Multi-Directional SS Maps*: At 7 GHz, Sionna was configured with TR38.901 directional antenna patterns oriented at eight principal angles  $\{0^\circ, 45^\circ, \dots, 315^\circ\}$ . For each Tx, eight SS maps were generated, representing beam-formed coverage in different directions. Fig. 4 shows an example set of directional maps  $\{\mathbf{S}_{d1}, \mathbf{S}_{d2}, \dots, \mathbf{S}_{d8}\}$ , showing beam concentration along pointing angles and variations caused by blockages. Table I highlights the parameters that differ from the 3.5 GHz configuration.

#### C. Data Preprocessing

To prepare the dataset for evaluation, several preprocessing steps were applied to ensure spatial consistency and representativeness of real-world measurement conditions. The

Table I  
SIMULATION PARAMETERS FOR GENERATING 3.5 GHz AND 7 GHz MAPS  
IN SIONNA. PARAMETERS NOT LISTED UNDER 7 GHz ARE IDENTICAL TO  
THOSE USED FOR 3.5 GHz.

Parameter	Value
Carrier frequency	3.5 GHz / 7 GHz
BS antenna height	Max building height + 5 m
UE antenna height	1.5 m
Number of rays	$3 \times 10^6$
BS antenna gain	0 dBi (3.5 GHz) / 6 dBi (7 GHz)
Reflection / Diffraction	Enabled / Enabled
Max reflection / diffraction order	8
Antenna pattern	Isotropic (3.5 GHz) / Directional (TR38.901) [28] (7 GHz)
Antenna polarization	Dual-polarized (VH)
Number of directions (7 GHz only)	8 ( $0^\circ, 45^\circ, \dots, 315^\circ$ )
Simulation area size	512 m $\times$ 512 m
Spatial resolution	4 m/pixel
Output resolution	128 $\times$ 128

procedure includes dataset partitioning, sparse sampling of 7 GHz maps, generation of LoS and non-line-of-sight (NLoS) masks, and synthesis of partially observed 3.5 GHz coverage maps.

1) *Dataset Partitioning*: A total of 3,721 building height maps were obtained from OSM and Blender modeling. Each was cropped into four subregions and downsampled to  $128 \times 128$ , yielding 14,884 building maps. For each valid sample, one building map  $\mathbf{B}$ , one 3.5 GHz coverage map  $\mathbf{S}_c$ , and eight directional 7 GHz SS maps  $\mathbf{S}_{d1}, \dots, \mathbf{S}_{d8}$  were required. Samples missing any of these components were discarded. The dataset was then split into training, validation, and test sets at a 7:2:1 ratio to ensure independence. Notably, the building maps used in the test set were completely disjoint from those in the training and validation sets, ensuring that model evaluation was performed on entirely unseen city blocks.

2) *Sparse 7 GHz SS Maps*: To emulate limited real-world measurements, sparse 7 GHz SS maps  $\{\tilde{\mathbf{S}}_{d1}, \dots, \tilde{\mathbf{S}}_{d8}\}$  were derived from the ground-truth  $\{\mathbf{S}_{d1}, \dots, \mathbf{S}_{d8}\}$  using two sampling strategies:

- *Random sampling*:  $N_d$  out of  $128 \times 128$  pixels were randomly selected, with the remaining pixels set to  $-160$  dBm.
- *NLoS-guided sampling*: Similar to the random sampling strategy,  $N_d$  pixels were selected, where a fraction  $\gamma$  was drawn from NLoS regions and  $(1 - \gamma)$  from LoS regions, prioritizing blocked areas.

Both strategies retained a resolution of  $128 \times 128$ , producing eight sparse maps per sample.

3) *LoS and NLoS Masks*: To better guide the model in learning blocked regions, LoS and NLoS masks, denoted as  $\mathbf{M}_{\text{LoS}}$  and  $\mathbf{M}_{\text{NLoS}}$ , were designed. The LoS mask  $\mathbf{M}_{\text{LoS}}$  is defined as a  $128 \times 128$  binary map with values of 0 or 1. It is computed using the Bresenham line algorithm. For each pixel  $(x_1, y_1)$  relative to a Tx at  $(x_0, y_0)$ , the connecting line is expressed as

$$y - y_0 = \frac{y_1 - y_0}{x_1 - x_0}(x - x_0), \quad (1)$$

and discretized into grid cells. If any cell (excluding the Tx) intersects a building, i.e.,  $[\mathbf{B}]_{x,y} > 0$ , the pixel is marked as

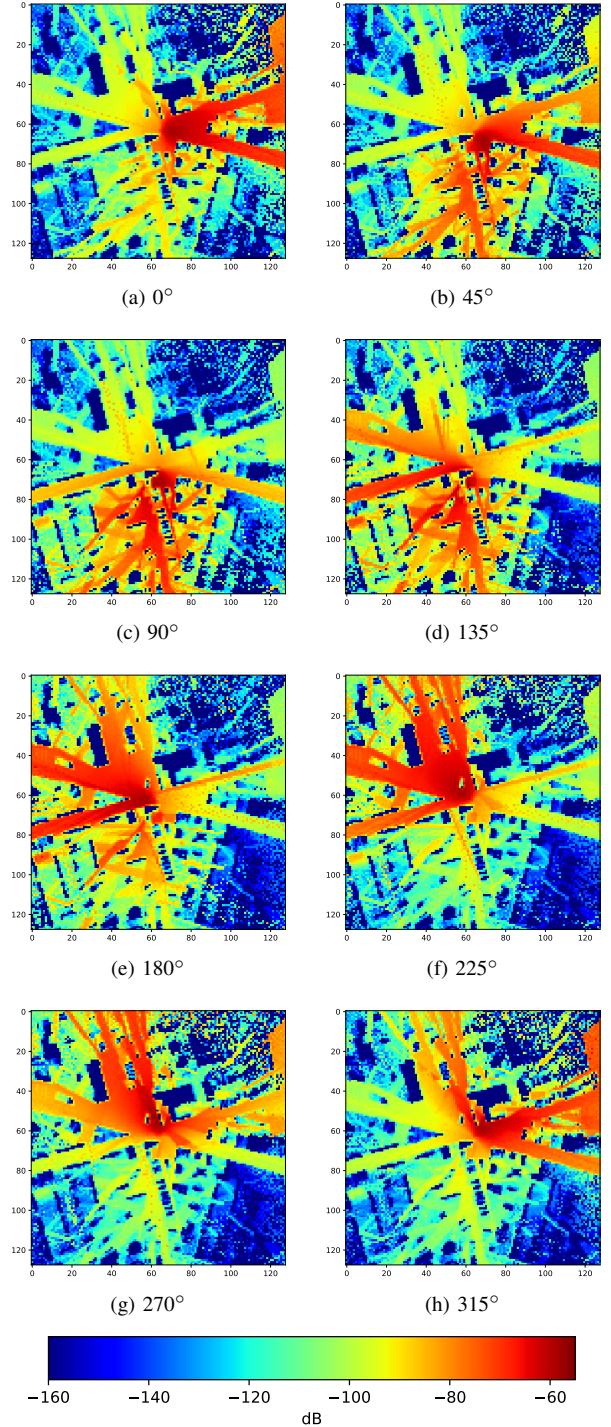


Figure 4. Eight generated 7 GHz SS maps  $\{\mathbf{S}_{d1}, \mathbf{S}_{d2}, \dots, \mathbf{S}_{d8}\}$ , showing beam concentration along pointing directions and variations caused by blockages.

blocked; otherwise, it is classified as LoS.

The NLoS mask  $\mathbf{M}_{\text{NLoS}}$  is defined as the complement of  $\mathbf{M}_{\text{LoS}}$ , with building interiors excluded. Hence,  $\mathbf{M}_{\text{LoS}}$  identifies pixels with unobstructed paths to the Tx, while  $\mathbf{M}_{\text{NLoS}}$  highlights free-space regions shadowed by buildings. Fig. 5 shows an example of the generated masks based on the building map in Fig. 3(a), where green pixels indicate LoS and red pixels indicate NLoS. During training,  $\mathbf{M}_{\text{NLoS}}$  is

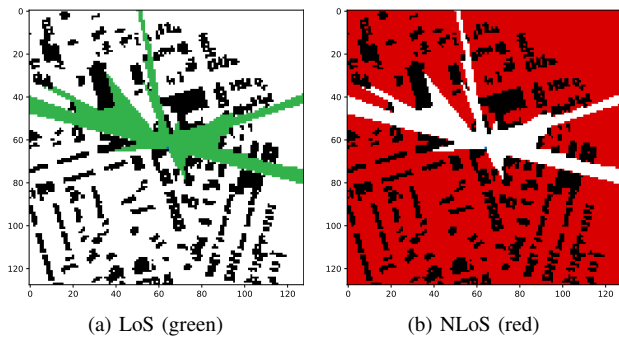


Figure 5. (a) LoS and (b) NLoS masks corresponding to the building map in Fig. 3(a).

incorporated as an additional input channel to improve feature learning in blocked areas.

4) *Sampled 3.5 GHz Maps*: To simulate scenarios in which the complete 3.5 GHz coverage map  $\mathbf{S}_c$  is unavailable, three variants  $\tilde{\mathbf{S}}_c$  were generated to represent different sampling conditions:

- **3.5 GHz Sparse Map**: Two sampling strategies were adopted to construct sparse low-frequency maps with  $N_c$  available pixels.
  - *Random sampling*:  $N_c$  pixels were uniformly selected at random, and the remaining pixels were assigned  $-160$  dBm.
  - *NLoS-guided sampling*: The same number of pixels was selected, with a fraction  $\gamma$  drawn from NLoS regions and  $(1 - \gamma)$  from LoS regions to emphasize blocked areas.
- **3.5 GHz Blend Map**: Starting from  $N_c$  sampled pixels ( $\gamma$  from NLoS and  $(1 - \gamma)$  from LoS regions), each selected value was expanded to its eight neighboring pixels (forming a nine-patch copy), resulting in  $9N_c$  pseudo-points. Overlapping values were resolved by prioritizing SS values  $\geq -90$  dBm or by averaging. Building pixels were set to  $-160$  dBm. This approach increases sampling density while preserving local spatial gradients.
- **3.5 GHz Block Map**: The map was divided into  $10 \times 10$  sliding blocks (14,161 in total), and the 10 blocks with the highest NLoS ratios were selected. Some pixels within these blocks corresponded to building interiors, which were not regions of interest. To compensate for these non-usable pixels, an equal number of non-building pixels was additionally sampled outside the selected blocks. Each map thus contained  $N_c$  sampled pixels, with greater emphasis on building edges and blockage regions.

Fig. 6 shows examples of blend and block maps generated from the coverage map in Fig. 3(b). The blend map preserves local gradients by expanding sparse samples, whereas the block map emphasizes NLoS-dominant regions around building edges.

#### IV. DATA-DRIVEN FRAMEWORK

The proposed framework addresses cross-band and multi-directional signal prediction. Two scenarios are considered

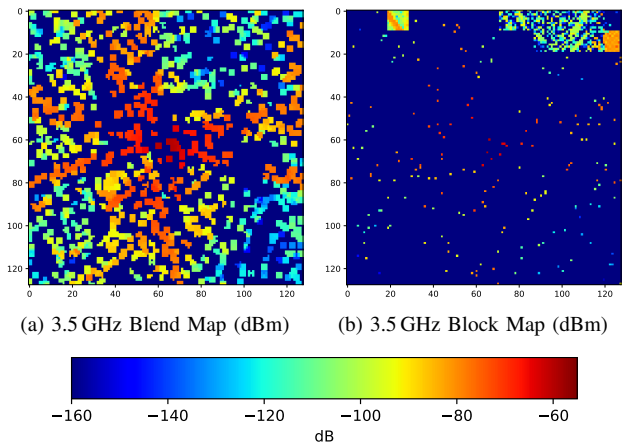


Figure 6. Examples of 3.5 GHz (a) blend and (b) block maps derived from the coverage map in Fig. 3(b).

depending on the availability of 3.5 GHz coverage data. In the **Full CommUNext** scenario, the complete 3.5 GHz map  $\mathbf{S}_c$  is available, providing strong reference information for cross-band learning. In the **Partial CommUNext** scenario, only sampled maps  $\tilde{\mathbf{S}}_c$  are accessible, and an auxiliary reconstruction strategy is introduced to compensate for missing data. This section first formulates the theoretical principle underlying cross-band and multi-directional prediction, and then presents the two neural architectures designed to approximate the Bayes-optimal solution.

##### A. Problem Formulation and Theoretical Principle

The task is formulated as a conditional estimation problem. Let

$$\mathcal{X} = \left\{ \mathbf{B}, \mathbf{S}_c \text{ (or } \tilde{\mathbf{S}}_c), \tilde{\mathbf{S}}_{d1}, \dots, \tilde{\mathbf{S}}_{ds} \right\}, \quad (2)$$

denote the available input tensor, where  $\mathbf{B}$  is the building height map,  $\mathbf{S}_c$  is the complete 3.5 GHz coverage map, and  $\{\tilde{\mathbf{S}}_{di}\}$  are sparse directional 7 GHz SS maps. The prediction target is the set of complete 7 GHz SS maps

$$\mathcal{Y} = \{\mathbf{S}_{d1}, \dots, \mathbf{S}_{ds}\}. \quad (3)$$

The objective is to learn a predictor  $f: \mathcal{X} \mapsto \hat{\mathcal{Y}}$  that minimizes the expected mean squared error (MSE):

$$\min_f \mathbb{E} [\|\mathcal{Y} - f(\mathcal{X})\|_F^2], \quad (4)$$

where  $\|\cdot\|_F$  denotes the Frobenius norm.<sup>2</sup>

*Theorem 1 (Bayes-Optimal Predictor under MSE [29]):* Under the MSE criterion, the Bayes-optimal predictor of  $\mathcal{Y}$  given  $\mathcal{X}$  is

$$f^*(\mathcal{X}) = \mathbb{E}[\mathcal{Y} | \mathcal{X}]. \quad (5)$$

Theorem 1 reveals two key principles: 1) the low-frequency coverage map  $\mathbf{S}_c$  (or its sampled counterpart  $\tilde{\mathbf{S}}_c$ ) provides a cross-band structural prior, encoding large-scale propagation geometry; 2) the sparse high-frequency maps  $\mathbf{S}_{di}$  serve as

<sup>2</sup>The Frobenius norm of an  $N$ -th order tensor  $\mathcal{Y} \in \mathbb{R}^{I_1 \times I_2 \times \dots \times I_N}$  is defined as the square root of the sum of the squares of all its elements.

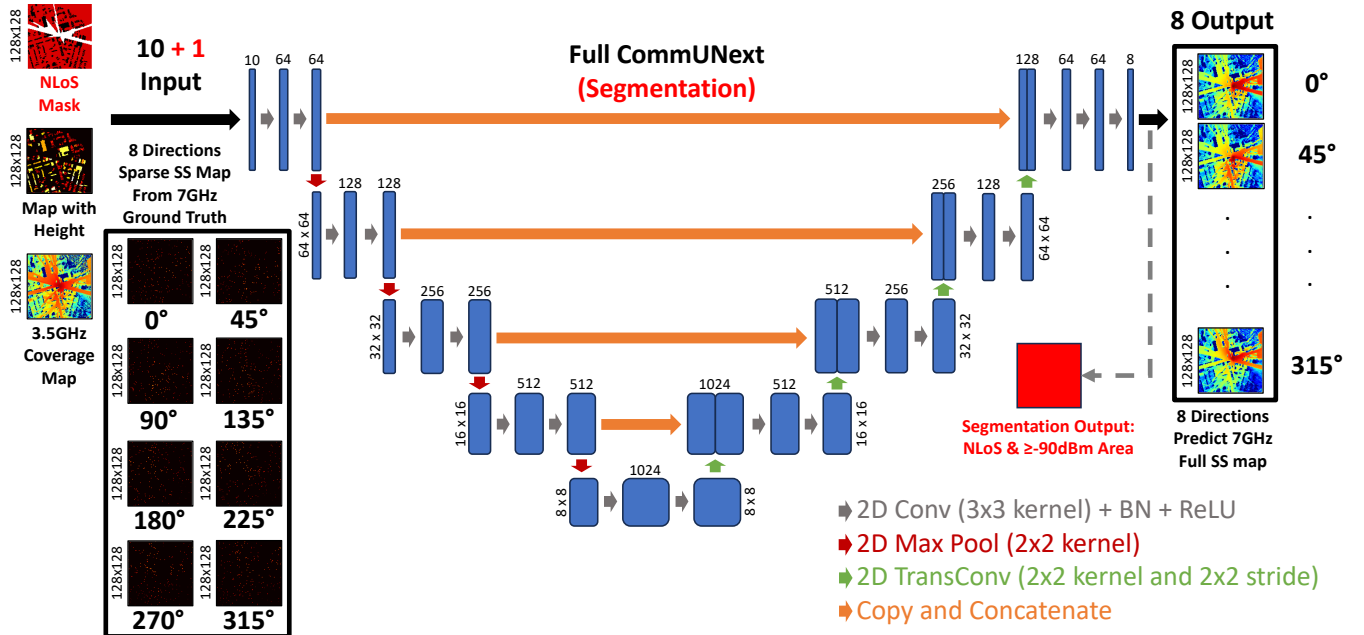


Figure 7. Full CommUNext and Seg architectures.

multi-directional anchors that capture orientation-dependent attenuation.

*Corollary 1 (Incomplete Reference-Band Case):* If  $\mathbf{S}_c$  is unavailable and only  $\tilde{\mathbf{S}}_c$  is observed, reconstructing

$$\hat{\mathbf{S}}_c \approx \mathbb{E} \left[ \mathbf{S}_c \mid \mathbf{B}, \tilde{\mathbf{S}}_c \right] \quad (6)$$

yields an MSE-optimal surrogate feature for the inner conditional, thereby enabling transfer of cross-band knowledge to enhance prediction performance.

**Proof:** When only  $\tilde{\mathbf{S}}_c$  is available, the Bayes-optimal predictor becomes

$$f^*(\mathbf{B}, \tilde{\mathbf{S}}_c, \{\tilde{\mathbf{S}}_{di}\}) = \mathbb{E} \left[ \mathcal{Y} \mid \mathbf{B}, \tilde{\mathbf{S}}_c, \{\tilde{\mathbf{S}}_{di}\} \right]. \quad (7)$$

By the law of iterated expectations,

$$\mathbb{E} \left[ \mathcal{Y} \mid \mathbf{B}, \tilde{\mathbf{S}}_c, \{\tilde{\mathbf{S}}_{di}\} \right] = \mathbb{E} \left[ g(\mathbf{B}, \mathbf{S}_c, \{\tilde{\mathbf{S}}_{di}\}) \mid \mathbf{B}, \tilde{\mathbf{S}}_c, \{\tilde{\mathbf{S}}_{di}\} \right], \quad (8)$$

where  $g(\mathbf{B}, \mathbf{S}_c, \{\tilde{\mathbf{S}}_{di}\}) \triangleq \mathbb{E} \left[ \mathcal{Y} \mid \mathbf{B}, \mathbf{S}_c, \{\tilde{\mathbf{S}}_{di}\} \right]$ . The equality in (8) follows from the tower property with latent  $\mathbf{S}_c$ . Using  $\hat{\mathbf{S}}_c = \mathbb{E}[\mathbf{S}_c \mid \mathbf{B}, \tilde{\mathbf{S}}_c]$  as an auxiliary input is MSE-optimal for estimating  $\mathbf{S}_c$  and serves as a practical surrogate to approximate the inner conditional. Exact sufficiency, however, would require additional structural assumptions (e.g., conditional linear-Gaussian models or an affine  $g$  in  $\mathbf{S}_c$ ). ■

### B. Full CommUNext

As stated in Theorem 1, when the complete 3.5 GHz coverage map  $\mathbf{S}_c$  is available, the optimal predictor is  $f^*(\mathbf{B}, \mathbf{S}_c, \{\tilde{\mathbf{S}}_{di}\}) = \mathbb{E}[\mathcal{Y} \mid \mathbf{B}, \mathbf{S}_c, \{\tilde{\mathbf{S}}_{di}\}]$ . The **Full CommUNext** network is designed to approximate this conditional expectation using a U-Net backbone extended for cross-band and multi-directional prediction.

The architecture of **Full CommUNext** is illustrated in Fig. 7. The input tensor is

$$\mathcal{X}_{\text{Full}} = \left\{ \mathbf{B}, \mathbf{S}_c, \tilde{\mathbf{S}}_{d1}, \dots, \tilde{\mathbf{S}}_{d8} \right\}. \quad (9)$$

The encoder applies stacked convolutions, batch normalization, and ReLU activations, followed by max pooling to extract hierarchical representations. The decoder performs transposed convolutions with skip connections, ensuring fusion of spatial and semantic features. The output is a set of eight reconstructed high-band SS maps

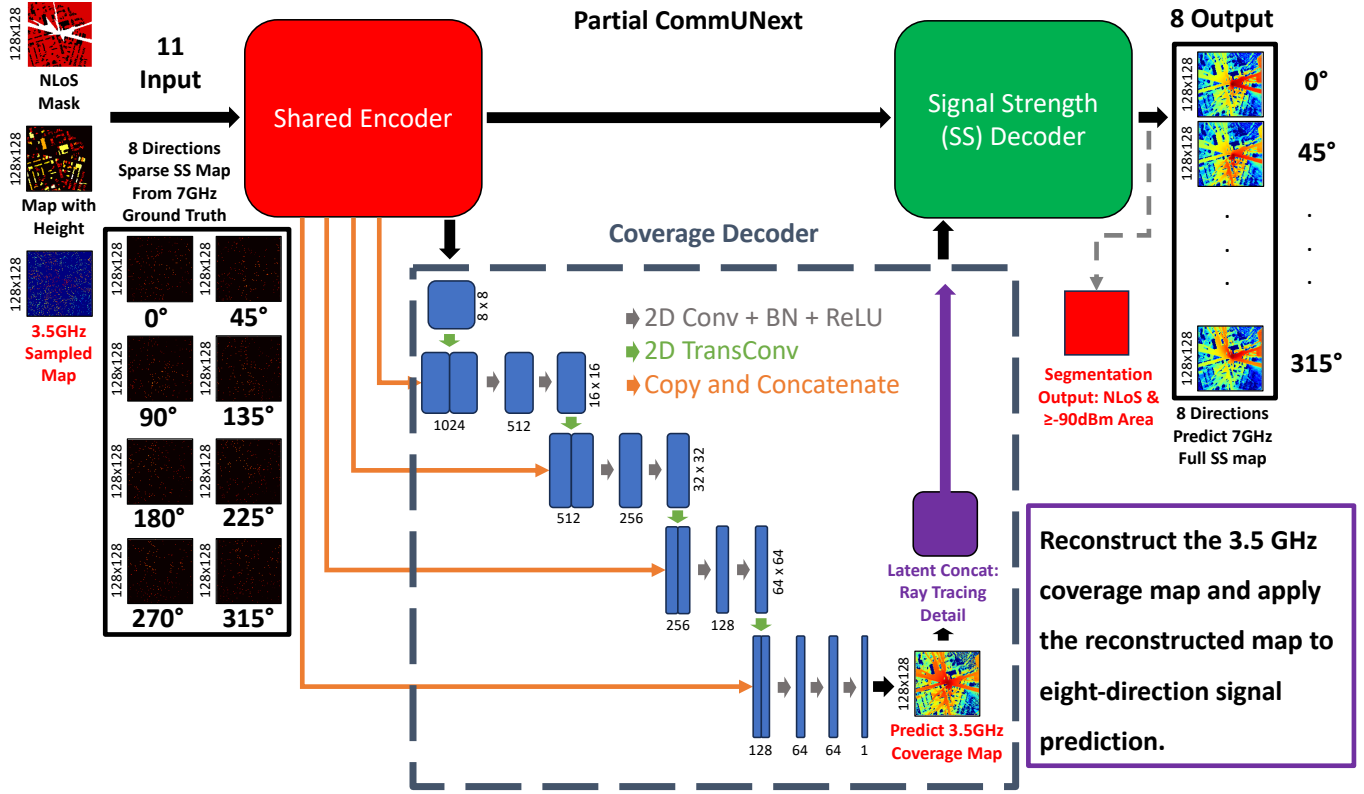
$$\hat{\mathcal{Y}} = \{ \hat{\mathbf{S}}_{d1}, \dots, \hat{\mathbf{S}}_{d8} \}. \quad (10)$$

To address blocked regions, the **Seg** extension incorporates an additional structured prior. The NLoS mask  $\mathbf{M}_{\text{NLoS}}$  is appended as an input channel, and a segmentation branch outputs  $\tilde{\mathbf{M}}_{\text{NLoS}}$ , which indicates communication-available NLoS pixels. This structured prior reduces prediction uncertainty in shadowed areas by constraining the feasible support of  $\mathcal{Y}$ .

The overall training objective combines regression and segmentation terms:

$$L_{\text{Full}} = L_{\text{SS}} + \lambda_{\text{Seg}} L_{\text{Seg}}, \quad (11)$$

where  $L_{\text{SS}}$  represents the MSE between the predicted high-band SS maps  $\hat{\mathcal{Y}} = \{ \hat{\mathbf{S}}_{di} \}$  and ground-truth SS maps  $\mathcal{Y} = \{ \mathbf{S}_{di} \}$ , and  $L_{\text{Seg}}$  denotes the binary cross-entropy (BCE) between the predicted and ground-truth NLoS masks. The weighting factor  $\lambda_{\text{Seg}}$  controls the contribution of the segmentation task. Notably, the error computations in  $L_{\text{SS}}$  are performed in the dB domain rather than the linear power domain, ensuring that errors are treated with equal importance. The linear domain would undervalue errors in weak-signal regions.


 Figure 8. **Partial CommUNext** architecture.

In summary, **Full CommUNext** realizes the Bayes predictor of Theorem 1 in practice by fusing complete low-frequency priors with sparse high-frequency directional anchors, while the **Seg** variant incorporates  $\mathbf{M}_{\text{NLoS}}$  as a structured prior to enhance robustness in NLoS regions.

*Remark 1 (Structured Prior via NLoS Mask):* The NLoS mask  $\mathbf{M}_{\text{NLoS}}$  provides structured prior knowledge by explicitly identifying shadowed but communication-available regions. Formally, conditioning on  $\mathbf{M}_{\text{NLoS}}$  reduces the predictive uncertainty of  $\mathcal{Y}$ :

$$\text{Var}(\mathcal{Y} | \mathcal{X}, \mathbf{M}_{\text{NLoS}}) \leq \text{Var}(\mathcal{Y} | \mathcal{X}), \quad (12)$$

where  $\mathcal{X}$  denotes the available inputs (either  $\mathcal{X}_{\text{Full}}$  or  $\mathcal{X}_{\text{Partial}}$ ). The inequality follows from the law of total variance, since  $\mathbf{M}_{\text{NLoS}}$  refines the conditional distribution of  $\mathcal{Y}$ . In practice, incorporating  $\mathbf{M}_{\text{NLoS}}$  as an input channel and training an auxiliary segmentation branch constrain predictions to feasible communication regions, improving robustness and reducing error in blocked areas.

### C. Partial CommUNext

Corollary 1 shows that when  $\mathbf{S}_c$  is unavailable, the optimal predictor depends on  $\{\mathbf{B}, \tilde{\mathbf{S}}_c, \tilde{\mathbf{S}}_{d1}, \dots, \tilde{\mathbf{S}}_{d8}\}$ , with latent reconstruction of  $\mathbf{S}_c$  required through  $\tilde{\mathbf{S}}_c \approx \mathbb{E}[\mathbf{S}_c | \mathbf{B}, \tilde{\mathbf{S}}_c]$ . A straightforward approach would be to design a separate coverage-reconstruction network and then feed the reconstructed 3.5 GHz map into the **Full CommUNext** model. However, this two-stage process is inefficient because the latent features used to reconstruct  $\mathbf{S}_c$  are not directly leveraged

for high-band prediction. Inspired by the dual-decoder design of Y-Net [30], the **Partial CommUNext** architecture introduces a coverage-reconstruction branch alongside the main SS prediction branch, as illustrated in Fig. 8.

The input tensor is

$$\mathcal{X}_{\text{Partial}} = \{\mathbf{B}, \tilde{\mathbf{S}}_c, \tilde{\mathbf{S}}_{d1}, \dots, \tilde{\mathbf{S}}_{d8}\}, \quad (13)$$

where  $\tilde{\mathbf{S}}_c$  is a sampled 3.5 GHz map (Sec. III-C4). The encoder is identical to **Full CommUNext**, ensuring consistent feature extraction. At the bottleneck, two decoders operate jointly:

- **Coverage Decoder:** Reconstructs  $\hat{\mathbf{S}}_c$  from  $\tilde{\mathbf{S}}_c$ , serving as an auxiliary task that approximates  $\mathbb{E}[\mathbf{S}_c | \mathbf{B}, \tilde{\mathbf{S}}_c]$  and transfers latent propagation knowledge.
- **SS Decoder:** Predicts the complete 7 GHz outputs  $\hat{\mathcal{Y}}$ , using skip connections and the reconstructed  $\hat{\mathbf{S}}_c$  as an auxiliary input. It also includes a segmentation branch that outputs  $\hat{\mathbf{M}}_{\text{NLoS}}$ , consistent with **Full CommUNext**.

The joint loss integrates three terms:

$$L_{\text{Partial}} = L_{\text{SS}} + \lambda_{\text{Seg}} L_{\text{Seg}} + \lambda_{\text{Cov}} L_{\text{Cov}}, \quad (14)$$

where  $L_{\text{Cov}}$  is the MSE between  $\hat{\mathbf{S}}_c$  and  $\mathbf{S}_c$ , and the weighting factor  $\lambda_{\text{Cov}}$  regulates its relative contribution.

In summary, **Partial CommUNext** operationalizes Corollary 1 by combining sampled low-band inputs with auxiliary coverage reconstruction, enabling effective approximation of the latent  $\mathbf{S}_c$  and thereby improving high-band SS prediction even under incomplete reference conditions.

## V. EXPERIMENTAL RESULTS

This section presents the analysis and discussion of the prediction performance of the proposed **Full CommUNext** and **Partial CommUNext** architectures. Evaluation is conducted by comparing the model predictions on the test set with the corresponding ground truth. Two error metrics are adopted: the mean absolute error (MAE) and the root mean squared error (RMSE):

$$\text{MAE} = \frac{1}{8N} \sum_{i=1}^8 \sum_{n=1}^N |\hat{S}_{di,n} - S_{di,n}|, \quad (\text{dB}) \quad (15a)$$

$$\text{RMSE} = \sqrt{\frac{1}{8N} \sum_{i=1}^8 \sum_{n=1}^N |\hat{S}_{di,n} - S_{di,n}|^2}, \quad (\text{dB}) \quad (15b)$$

where  $\hat{S}_{di,n}$  and  $S_{di,n}$  denote the predicted and ground-truth dBm values of the  $n$ -th pixel in  $\mathbf{S}_{di}$ , respectively, and  $N$  represents the number of pixels of each ground-truth map.

Beyond average performance, the statistical distribution of prediction errors is examined using box plots of MAE and RMSE (see Fig. 9 as an example). As illustrated in Fig. 9, the interquartile range (IQR) quantifies the variability of errors and is defined as the difference between the third quartile ( $Q_3$ ) and the first quartile ( $Q_1$ ):

$$\text{IQR} = Q_3 - Q_1, \quad (16)$$

representing the range covering the central 50% of the data. A larger IQR indicates greater dispersion of the main error distribution, whereas a smaller IQR implies that errors are more concentrated around the median. In box plots, the lower whisker (L-Whisker) extends to the smallest point within  $Q_1 - 1.5 \times \text{IQR}$ , and the upper whisker (U-Whisker) extends to the largest point within  $Q_3 + 1.5 \times \text{IQR}$ . Data points outside this range are considered outliers and typically correspond to rare but extreme prediction errors.<sup>3</sup>

From a practical standpoint, a large difference between the IQRs of MAE and RMSE indicates that outliers significantly skew the error distribution. Conversely, similar IQRs imply a more uniform error distribution and better model robustness to extreme deviations. Therefore, joint consideration of MAE, RMSE, and IQR provides a comprehensive assessment of both the accuracy and stability of the proposed architectures.

In the **Full CommUNext** experiments, the model's prediction capability is evaluated using the complete 3.5 GHz coverage map as input. Three aspects are analyzed in detail: (i) performance before and after architectural optimization, (ii) the effect of reducing the number of 7 GHz directional inputs, and (iii) the impact of different 7 GHz sampling strategies. For the **Partial CommUNext** experiments, the focus is on assessing the reconstruction of the 3.5 GHz coverage map under incomplete coverage conditions. By generating input maps through various sparse-sampling strategies, we further

<sup>3</sup>Only pixels within the communicable region are analyzed in the box plots, since including outliers in non-communicable regions is meaningless. A communicable point is defined as a pixel satisfying  $S_{di,n} \geq -90$  dBm, corresponding to the approximate thermal noise level at 300 K, 100 MHz bandwidth, and 4 dB noise figure ( $-90$  dBm).

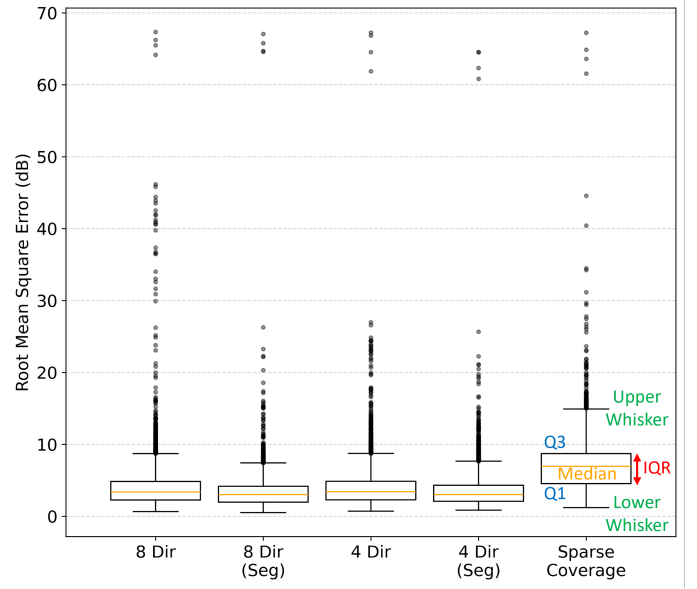


Figure 9. Box plots of RMSE for **Full CommUNext** under different numbers of directional inputs.

analyze how different sampling patterns affect the overall prediction accuracy and robustness of the model.

#### A. Full CommUNext (With Complete 3.5 GHz Coverage Map)

1) *Model Optimization Comparison:* **Full CommUNext** is evaluated using two network variants introduced in Section IV-B. The baseline U-Net employs only the regression loss  $L_{SS}$  in (11), focusing solely on the prediction accuracy of SS maps. The extended **Seg** architecture, by contrast, incorporates the NLoS mask  $\mathbf{M}_{NLoS}$  as an additional input channel and activates the segmentation branch. In this configuration,  $L_{Seg}$  is included with a weighting factor of  $\lambda_{Seg} = 0.3$ , resulting in a multi-task objective that jointly optimizes SS reconstruction and NLoS mask prediction.

Five experimental settings are designed to evaluate the effectiveness of the Seg architecture and to test the core hypothesis of **Full CommUNext**: whether reliable high-frequency predictions can still be achieved when some directional inputs are missing, guided by low-frequency features.

- i. **8 Dir:** All eight 7 GHz sparse SS maps are used.
- ii. **8 Dir (Seg):** Same as 8 Dir, but with the Seg branch enabled.
- iii. **4 Dir:** Only four sparse SS maps ( $0^\circ$ ,  $90^\circ$ ,  $180^\circ$ ,  $270^\circ$ ) are used.
- iv. **4 Dir (Seg):** Same as 4 Dir, but with the Seg branch enabled.
- v. **Sparse Coverage:** The complete 3.5 GHz coverage map is unavailable; only sparse-sampled 3.5 GHz maps are provided.

In these experiments, each 7 GHz sparse SS map  $\tilde{\mathbf{S}}_{di}$  contains  $N_d = 200$  randomly sampled pixels, and each sparse-sampled 3.5 GHz map  $\tilde{\mathbf{S}}_c$  contains  $N_c = 1,000$  randomly sampled pixels.

Table II summarizes MAE and RMSE across settings. To better interpret these values, Fig. 9 presents the corresponding

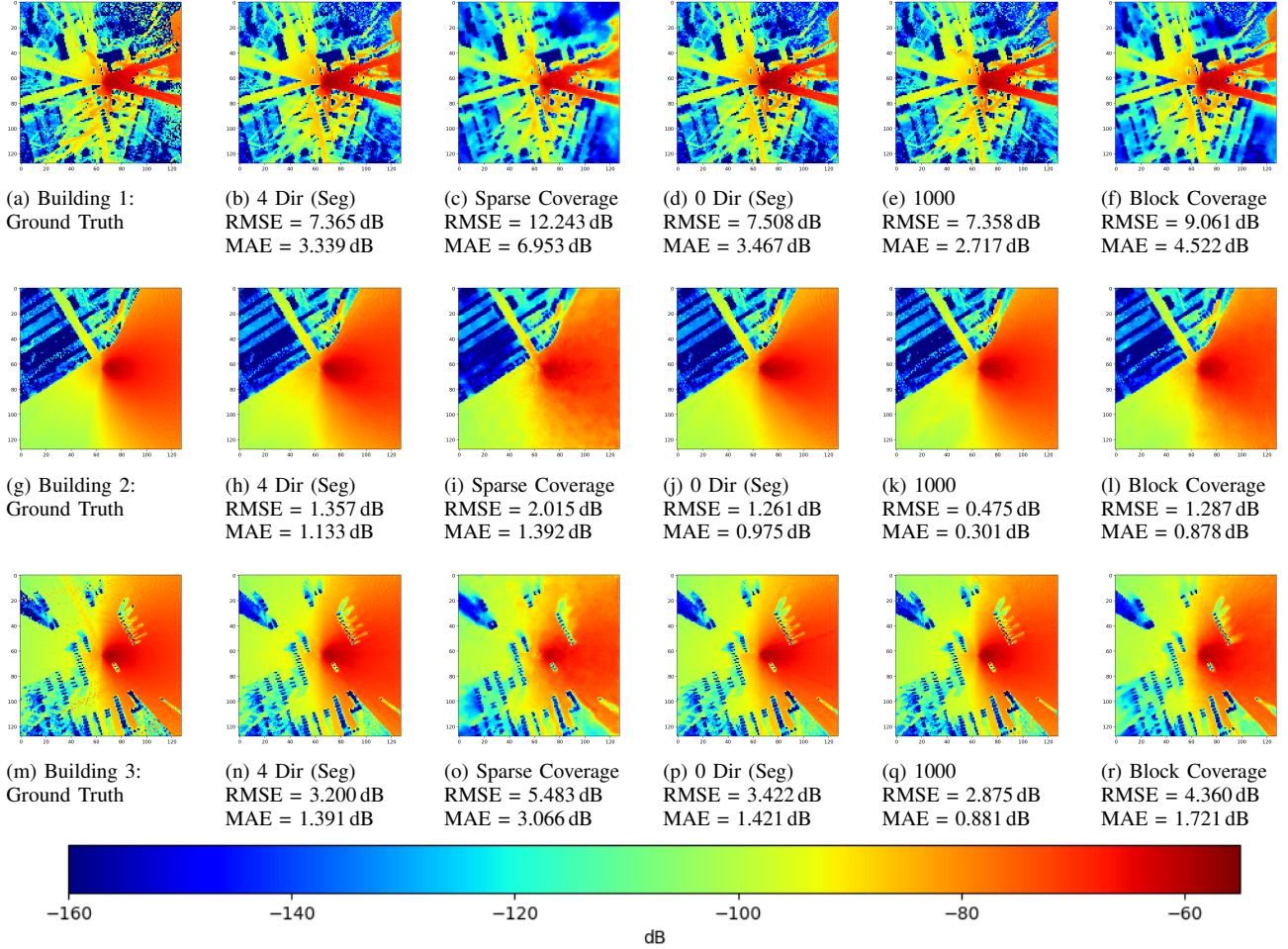


Figure 10. Comparison between ground truth and predictions under different conditions for three test maps (restricted to ground-truth regions with  $SS \geq -90$  dBm).

Table II  
MODEL OPTIMIZATION RESULTS WITHIN THE COMMUNICABLE REGION: MAE AND RMSE.

Case	MAE						RMSE					
	Q1	Q3	IQR	Median	L-Whisker	U-Whisker	Q1	Q3	IQR	Median	L-Whisker	U-Whisker
8 Dir	1.227	2.641	1.414	1.797	0.461	4.759	2.264	4.854	2.589	3.367	0.657	8.727
8 Dir (Seg)	1.037	2.076	1.039	1.489	0.409	3.634	1.974	4.161	2.187	3.011	0.518	7.426
4 Dir	1.297	2.679	1.383	1.859	0.520	4.752	2.292	4.873	2.581	3.411	0.722	8.744
4 Dir (Seg)	1.305	2.421	1.116	1.717	0.627	4.094	2.076	4.316	2.240	3.011	0.844	7.672
Sparse Coverage	2.563	5.631	3.069	4.371	0.924	10.202	4.550	8.728	4.178	6.940	1.205	14.907

Table III  
DIRECTIONAL (ANGLE) COMPARISON WITHIN THE COMMUNICABLE REGION: MAE AND RMSE.

Case	MAE						RMSE					
	Q1	Q3	IQR	Median	L-Whisker	U-Whisker	Q1	Q3	IQR	Median	L-Whisker	U-Whisker
4 Dir (Seg)	1.305	2.421	<b>1.115</b>	1.716	0.627	4.094	2.075	4.315	2.240	3.011	0.843	7.671
2 Dir (Seg)	1.176	2.424	1.248	1.674	0.428	4.296	2.068	4.507	2.438	3.131	0.605	8.164
1 Dir (Seg)	1.110	2.349	1.238	1.599	0.455	4.204	1.981	4.397	2.416	3.042	0.632	8.016
1 Random (Seg)	1.044	2.318	1.273	1.550	0.342	4.225	1.959	4.391	2.432	3.038	0.472	8.036
0 Dir (Seg)	1.265	2.483	1.218	1.744	0.566	4.309	2.150	4.577	2.426	3.182	0.753	8.201

box plots of RMSE. Within the communicable region, the **Seg** architecture consistently outperforms the baseline. Notably, **4 Dir (Seg)** surpasses **8 Dir** without segmentation, indicating the benefit of the auxiliary branch. Using eight directions is still slightly better than four in both designs, but the gaps are small, which suggests robustness to missing directional inputs. In contrast, **Sparse Coverage** exhibits clear degradation when

a complete 3.5 GHz map is not available, underscoring the role of low-frequency coverage as guidance and motivating the **Partial CommUNext** design.

Moreover, from the MAE and RMSE statistics in Table II, we also observe that both **8 Dir** and **8 Dir (Seg)** exhibit smaller errors across multiple indicators, suggesting not only a downward shift in the overall error distribution but also a

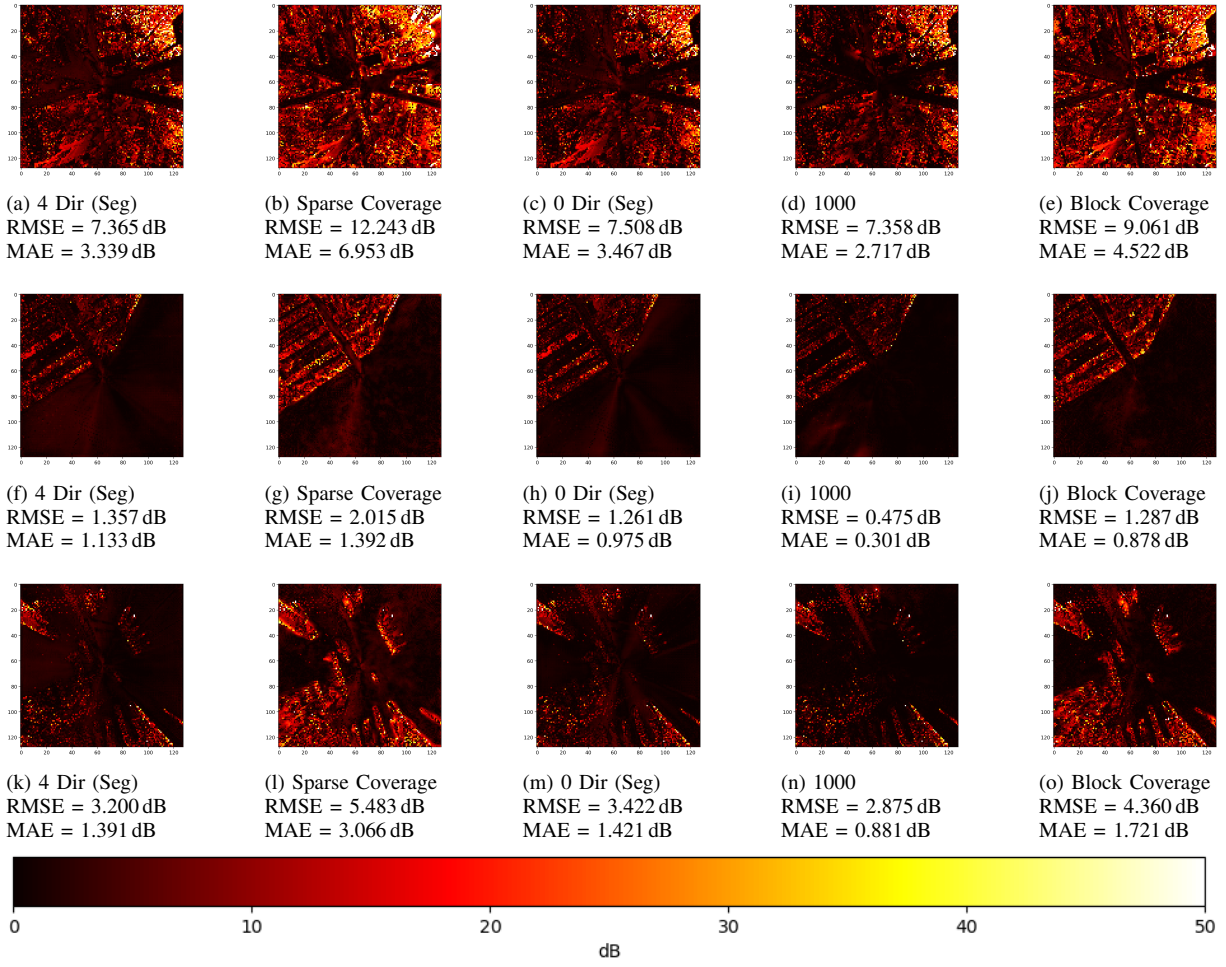


Figure 11. Absolute error maps under different conditions for three test maps.

 Table IV  
 NLOS SPARSE SAMPLING COMPARISON WITHIN THE COMMUNICABLE REGION: MAE AND RMSE.

Case	MAE						RMSE					
	Q1	Q3	IQR	Median	L-Whisker	U-Whisker	Q1	Q3	IQR	Median	L-Whisker	U-Whisker
200	0.721	1.864	1.142	1.209	0.112	3.578	1.739	4.046	2.306	2.832	0.153	7.501
400	0.721	1.805	1.084	1.190	0.158	3.431	1.702	3.911	2.208	2.751	0.215	7.219
600	0.719	1.744	1.024	1.171	0.165	3.279	1.665	3.770	2.105	2.670	0.222	6.922
800	0.719	1.729	1.009	1.169	0.174	3.241	1.645	3.695	2.049	2.623	0.239	6.760
1000	0.737	1.704	0.967	1.164	0.190	3.150	1.618	3.604	1.986	2.567	0.265	6.581

 Table V  
 COMPARISON OF 3.5 GHz SAMPLING STRATEGIES WITHIN THE COMMUNICABLE REGION: MAE AND RMSE.

Case	MAE						RMSE					
	Q1	Q3	IQR	Median	L-Whisker	U-Whisker	Q1	Q3	IQR	Median	L-Whisker	U-Whisker
Sparse Random	1.912	4.239	2.327	3.233	0.652	7.704	3.645	7.097	3.451	5.547	0.861	12.271
Sparse NLoS	1.934	4.186	2.252	3.180	0.647	7.538	3.634	6.920	3.286	5.449	0.884	11.849
Blend Coverage	2.024	4.476	2.452	3.386	0.623	8.138	3.758	7.290	3.532	5.746	0.853	12.575
Block Coverage	1.744	4.025	2.281	2.975	0.579	7.432	3.380	6.796	3.415	5.308	0.759	11.904
Full CommUNext	2.563	5.631	3.069	4.371	0.924	10.202	4.550	8.728	4.178	6.940	1.205	14.907

reduction or suppression of outliers. A similar trend can be found when comparing **4 Dir** and **4 Dir (Seg)**. In contrast, **Sparse Coverage** shows considerably higher MAE and RMSE values than the other four cases, reflecting that the absence of the 3.5 GHz coverage map leads to an overall increase in prediction error as well as a larger presence of outliers.

To illustrate practical behavior, three representative cases are selected from 1,479 test maps, covering dense urban, single-

block, and sparse-building areas. Fig. 10 compares predicted 7 GHz SS maps at  $0^\circ$  with ground truth, and Fig. 11 shows the corresponding absolute error:

$$e_{di,n} = \left| \widehat{S}_{di,n} - S_{di,n} \right| \quad (\text{dB}), \quad (17)$$

where  $e_{di,n}$  is the pixelwise absolute error. Darker colors indicate smaller errors; lighter colors from red to yellow to white indicate larger errors. Most large errors occur in NLoS

open areas and near building edges within NLoS regions. Overall, predictions are accurate in most areas, especially along LoS paths and antenna beam lobes. Results for **Sparse Coverage** (Fig. 10(c), (i), (o)) show visible degradation without complete 3.5 GHz maps, including reduced detail in NLoS open areas and less accurate boundaries in strong and weak beam directions. The error maps (Fig. 11(b), (g), (l)) confirm substantial increases in these regions, reinforcing the need for low-frequency coverage to support cross-band prediction.

2) *7 GHz Directional (Angle) Comparison:* The previous results demonstrated that the model maintains directional completion capability even when the eight-direction 7 GHz sparse SS inputs are reduced to four. To further examine the effect of directional sparsity, we evaluate performance using fewer input directions. Building upon the best-performing **Seg** architecture, five configurations are tested by varying the number of 7 GHz sparse SS input directions:

- i. **4 Dir (Seg):**  $0^\circ, 90^\circ, 180^\circ, 270^\circ$ .
- ii. **2 Dir (Seg):**  $0^\circ, 180^\circ$ .
- iii. **1 Dir (Seg):**  $0^\circ$ .
- iv. **1 Random (Seg):** One randomly selected from the eight canonical directions.
- v. **0 Dir (Seg):** No high-frequency directional input; the model relies on the remaining inputs.

The results indicate that reducing the number of high-frequency directional inputs does not cause substantial degradation. Although **4 Dir (Seg)** provides more directional cues, it may introduce minor instability when sparse samples are drawn from challenging areas. **1 Random (Seg)** achieves robust performance, likely because sample-wise directional diversity enriches the learned angular features. Remarkably, **0 Dir (Seg)** still reconstructs the eight-direction 7 GHz SS maps with *reasonable* accuracy. This can be attributed to the fact that the eight canonical directions are fixed across all samples, thereby reducing the necessity of explicit directional anchors for orientation calibration.

In Table III, we primarily compare the differences between **4 Dir (Seg)** and **0 Dir (Seg)** within the communicable region. It can be observed that although **0 Dir (Seg)** shows a slightly less concentrated distribution in both MAE and RMSE, the RMSE results further indicate that the absence of directional high-frequency samples in some regions leads to larger prediction errors. Consequently, the median and several other statistical indicators of **0 Dir (Seg)** are marginally higher than those of **4 Dir (Seg)**, which is an expected outcome. Nevertheless, the MAE performance across the two settings remains close, suggesting that their overall error distributions are comparable. This demonstrates that the proposed method can still achieve reliable prediction accuracy even in scenarios with missing high-frequency directional inputs.

Illustrative predictions for **0 Dir (Seg)** are shown in Fig. 10(d), (j), (p), with corresponding absolute error maps in Fig. 11(c), (h), (m), where darker tones indicate lower errors in open LoS areas and beam lobes, highlighting the architecture's cross-band and multi-directional completion capability.

3) *7 GHz Sparse Sampling Strategy Comparison:* As discussed in the previous subsection, the model can reconstruct eight-direction SS maps even in the absence of high-frequency

directional inputs. We now investigate whether different sampling strategies can improve performance under a fixed total sample size. Observations from the previous analyses indicate that major prediction errors tend to occur in NLoS open regions. Therefore, we adopt the *NLoS-guided sampling* strategy described in Section III-C2, where each 7 GHz sparse SS map is constructed by selecting a fixed number of sampling points, with  $\gamma = 90\%$  drawn from NLoS open regions and 10% from LoS, non-building regions. The sampling densities are configured as  $N_d = 200, 400, 600, 800,$  and 1000 points per map, respectively.

We first compare the prediction results when switching the 7 GHz Sparse SS map generation strategy from Random Sampling to NLoS-guided sampling. Using the same setting of 200 sampled points per map across eight directions, we contrast the results of **8 Dir (Seg)** in Table II with the **200** case in Table IV. The results reveal that NLoS-guided sampling consistently yields lower MAE and RMSE across multiple indicators, indicating not only a downward shift in the overall error distribution but also a reduction or suppression of outliers. Furthermore, by examining the NLoS-guided sampling results in Table IV from 200 up to 1000 sampled points per map, we observe a gradual decrease in both the median MAE and RMSE, with the best performance achieved at 1000 points. This confirms that denser sampling within NLoS open regions, where errors are typically largest, further reduces outliers and improves overall prediction accuracy.

As shown in Fig. 10(e), (k), (q) and Fig. 11(d), (i), (n), predictions are most accurate under the 1000-point setting, with reduced error concentrations.

4) *Discussion:* The three sets of experiments under **Full CommUNext** lead to the following observations:

- **Cross-band and multi-directional prediction:** Leveraging complete low-frequency coverage with high-frequency sparse samples enables learning of inter-band and inter-directional correspondences.
- **Seg architecture advantage:** Incorporating NLoS masks with multi-task learning improves accuracy over the baseline U-Net.
- **No high-frequency inputs:** The model can reconstruct reasonable eight-direction SS maps without high-frequency directional data, showing generalization under unknown band and direction conditions.
- **Dense NLoS sampling:** Increasing sample density in NLoS open regions substantially reduces errors and improves robustness.
- **Role of low-frequency coverage:** Complete 3.5 GHz maps provide essential context for reliable predictions. The **Sparse Coverage** results show that lacking full low-frequency maps degrades performance significantly, motivating **Partial CommUNext** for scenarios with incomplete low-frequency coverage.

## B. Partial CommUNext (Incomplete 3.5 GHz Coverage Map)

1) *3.5 GHz Sampling Strategy Comparison:* To address realistic scenarios where complete low-frequency coverage maps are unavailable, we adopt the **Partial CommUNext** architecture introduced in Section IV-C, together with the 3.5 GHz

Table VI  
COMPARISON OF MEDIAN MAE/RMSE UNDER FOUR SAMPLING SCENARIOS WITHIN THE COMMUNICABLE REGION.

Case	3.5 GHz & 7 GHz Sampled		Only 3.5 GHz Sampled		Only 7 GHz Sampled		Neither Sampled	
	MAE <sub>med</sub>	RMSE <sub>med</sub>	MAE <sub>med</sub>	RMSE <sub>med</sub>	MAE <sub>med</sub>	RMSE <sub>med</sub>	MAE <sub>med</sub>	RMSE <sub>med</sub>
Sparse Random	1.709	2.055	2.067	3.354	2.016	2.867	3.348	5.614
Sparse NLoS	1.602	1.941	1.947	3.123	1.884	2.632	3.263	5.574
Blend Coverage	2.149	2.962	2.958	4.735	2.163	2.989	3.813	6.400
Block Coverage	1.582	2.031	1.995	3.506	1.849	2.627	3.181	5.531
Full CommUNext	2.112	2.602	4.327	6.818	2.445	3.404	4.372	6.941

sampling strategies described in Section III-C4. Sparse maps are generated from the 3.5 GHz coverage data using  $N_c = 1,000$  samples and  $\gamma = 90\%$  under different strategies, and are provided as inputs during training. Five configurations are considered:

- i. **Sparse Random:** Random sampling, identical to the Sparse Coverage case in **Full CommUNext**.
- ii. **Sparse NLoS:** Sampling guided by NLoS regions.
- iii. **Blend Coverage:** Pseudo-point expansion from initial samples to higher density.
- iv. **Block Coverage:** Block-based sampling targeting NLoS regions.
- v. **Full CommUNext:** Results from the Sparse Coverage case in **Full CommUNext**, included for comparison.

All configurations are applied to the 3.5 GHz coverage maps, rather than to the 7 GHz data. The objective is to determine which 3.5 GHz sparse-map strategy best compensates for missing complete coverage. For the 7 GHz input, four fixed directional sparse SS maps ( $0^\circ$ ,  $90^\circ$ ,  $180^\circ$ , and  $270^\circ$ ) are used, each containing  $N_d = 200$  randomly sampled pixels per direction. All **Partial CommUNext** experiments are trained with  $\lambda_{\text{Seg}} = 0.3$  and  $\lambda_{\text{Cov}} = 0.5$  in (14).

Table V compares the **Sparse Random** case with the **Full CommUNext** baseline, where both settings use identical 3.5 GHz sparse maps with random sampling. The results show that **Partial CommUNext** achieves superior prediction accuracy under this setting. Furthermore, **Sparse NLoS** consistently outperforms **Sparse Random**, confirming that directing samples toward challenging NLoS regions provides valuable guidance for high-frequency prediction. In contrast, **Blend Coverage**, although increasing the number of pseudo-points, introduces cumulative errors that ultimately degrade performance relative to direct sparse maps. By comparison, **Block Coverage** achieves the best results, striking a balance between sampling difficult NLoS areas and preserving structural features, thereby enabling finer reconstruction of local propagation characteristics.

In addition, the MAE and RMSE values in Table V reveal that while the differences across the four **Partial CommUNext** cases are relatively small in terms of MAE, the RMSE upper whiskers for **Sparse NLoS** and **Block Coverage** are notably lower than those for **Sparse Random** and **Blend Coverage**. This indicates that sampling more points from NLoS and other challenging regions not only reduces overall errors but also suppresses the occurrence of large outliers. On the other hand, although **Blend Coverage** also draws most points from NLoS regions, the replicated pseudo-points may mislead the model

and introduce larger prediction errors, leading to inferior performance.

Furthermore, Table VI refines the results of Table V by separating performance according to whether prediction is assisted by a 3.5 GHz sampled point, a 7 GHz sparse SS point (at other directions), both, or neither. The results exhibit a consistent trend: configurations combining 7 GHz sparse SS samples with 3.5 GHz sampled points achieve the highest accuracy, followed by those using only 7 GHz sparse SS points. In this setting, even a single 7 GHz sparse SS point provides directional cues that help reconstruct SS values across all other directions at 7 GHz. Using only 3.5 GHz sampled points ranks third but still reduces errors through cross-band guidance. Comparing the cases of using only 7 GHz versus only 3.5 GHz inputs, it is evident that a 7 GHz sparse SS point provides richer information than a 3.5 GHz sampled point, since the 7 GHz observation lies in the target band, even if only one directional cue is available. As expected, the absence of both reference sources yields the worst performance, where predictions rely primarily on spatial correlations inferred from nearby users. Notably, the median MAE and RMSE of the **Neither Sampled** case are close to, but slightly worse than, the aggregate values in Table V. This occurs because most pixels belong to the **Neither Sampled** category, while the relatively few pixels with 3.5 GHz or 7 GHz samples contribute marginal improvements, leading to the observed discrepancy.

2) *Qualitative Evaluation and Discussion:* Fig. 10(f), (l), (r) show predictions using the 3.5 GHz Block Coverage strategy. Compared with the **Sparse Coverage** case in Fig. 10(c), (i), (o), the block sampling better preserves RT path structures. For instance, the upper-right region in Fig. 10(f) exhibits improved reconstruction, indicating that block-wise sampling enhances local feature retention and leads to higher overall prediction quality. The corresponding error maps in Fig. 11(e), (j), (o) further confirm reduced errors in NLoS open regions compared with **Full CommUNext** with Sparse Coverage in Fig. 11(b), (g), (l).

Overall, although **Partial CommUNext** cannot match the precision of **Full CommUNext** with complete 3.5 GHz coverage, it consistently outperforms **Full CommUNext** when only sampled maps are available. By integrating well-designed sampling strategies, **Partial CommUNext** can effectively reconstruct 3.5 GHz maps and predict complete eight-direction 7 GHz SS maps, underscoring its strong practical potential in real-world scenarios where full low-frequency coverage is unavailable. Several conclusions can be drawn:

- **Partial CommUNext vs. Full CommUNext:** Under

identical sampling maps, **Partial CommUNext** achieves superior prediction compared with **Full CommUNext**, as evidenced by the **Sparse Random** case.

- **NLoS-guided sampling improves accuracy: Sparse NLoS** outperforms **Sparse Random**, confirming that sampling difficult NLoS regions provides valuable guidance for high-frequency prediction.
- **Block-based sampling balances difficulty and structure: Block Coverage** yields the best results, capturing NLoS areas while preserving structural features and enabling finer reconstruction of local propagation characteristics.
- **Practical potential of Partial CommUNext:** While not as precise as **Full CommUNext** with full coverage, **Partial CommUNext** combined with appropriate sampling strategies can reconstruct 3.5 GHz maps and predict complete eight-direction 7 GHz SS maps, offering strong applicability to real-world scenarios where full low-frequency coverage is unavailable.

## VI. CONCLUSION

This study proposed **CommUNext**, a deep learning framework capable of cross-band and multi-directional prediction, and validated its performance under different levels of data completeness. Experimental results demonstrate that, when a complete low-frequency 3.5 GHz coverage map is available, the **Full CommUNext** effectively assists the model in predicting multi-directional high-frequency 7 GHz SS maps. Even in scenarios with sparse high-frequency directional data or incomplete low-frequency information, the model maintains reasonable prediction capability. To address the practical challenge of obtaining complete low-frequency coverage maps, we further designed the **Partial CommUNext** architecture, which leverages different sampling strategies to reconstruct the low-frequency coverage map from limited 3.5 GHz samples, and subsequently predicts the high-frequency SS distribution based on this reconstructed map. Overall, this work demonstrates that efficient and robust communication prediction can be achieved under constrained data conditions through architectural and sampling design. It holds practical potential for future cross-band and multi-directional beam prediction, urban map-aware communication datasets, and real-time intelligent deployment and dynamic resource allocation in next-generation systems.

## REFERENCES

- [1] S. Kang *et al.*, “Cellular wireless networks in the upper mid-band,” *IEEE Open Journal of the Communications Society*, vol. 5, pp. 2058–2075, 2024.
- [2] ITU-R, “Framework and overall objectives of the future development of IMT for 2030 and beyond,” International Telecommunication Union Radiocommunication Sector (ITU-R), Tech. Rep., Sep. 2023. [Online]. Available: <https://www.itu.int/en/ITU-R/study-groups/rsg5/rwp5d/imt-2030/Pages/default.aspx>
- [3] NVIDIA, “Sionna,” <https://nvlabs.github.io/sionna/index.html>, 2025, accessed: Aug. 18, 2025.
- [4] Remcom, “Wireless insite 3d wireless propagation software,” <https://www.remcom.com/wireless-insite-propagation-software>, 2024.
- [5] 3GPP, *NR; Radio Resource Control (RRC); Protocol Specification*, Std. TS 38.331, 2025.
- [6] —, *NR; Requirements for Support of Radio Resource Management*, Std. TS 38.133, 2018.
- [7] 5G Americas, “Evolution of 5G spectrum: Purpose and background,” Tech. Rep., Feb. 2024. [Online]. Available: <https://www.5gamericas.org/wp-content/uploads/2024/01/BP-Evolution-of-5G-Spectrum.pdf>
- [8] Ericsson. (2025, Jun.) 6G standardization: The technology realization step begins. [Online]. Available: <https://www.ericsson.com/en/blog/2025/6/blog-6g-standardization-technology-step-to-publish>
- [9] Y. Li *et al.*, “A generalized deep learning model for signal coverage prediction in the CBRS band,” in *Proc. IEEE Int. Symp. Dynamic Spectrum Access Networks (DySPAN)*, 2025, pp. 1–5.
- [10] Y. Ma *et al.*, “Dual-GRE: Dual-phase enhancement in radiomap estimation based on graph attention,” *IEEE Wireless Communications Letters*, vol. 14, no. 8, pp. 2646–2650, 2025.
- [11] L. Liu *et al.*, “PINN and GNN-based RF map construction for wireless communication systems,” *arXiv preprint arXiv:2507.22513*, 2025. [Online]. Available: <https://arxiv.org/abs/2507.22513>
- [12] R. Levie *et al.*, “RadioUNet: Fast radio map estimation with convolutional neural networks,” *IEEE Transactions on Wireless Communications*, vol. 20, no. 6, pp. 4001–4015, Jun. 2021.
- [13] Y. Li *et al.*, “GeoSigMap: High-fidelity rf signal mapping using geographic databases,” in *Proc. IEEE Int. Symp. Dynamic Spectrum Access Networks (DySPAN)*, Washington, DC, USA, 2024, pp. 277–285.
- [14] K. Qiu *et al.*, “Pseudo ray-tracing: Deep learning assisted outdoor mm-wave path loss prediction,” *IEEE Wireless Communications Letters*, vol. 11, no. 8, pp. 1699–1702, Aug. 2022.
- [15] Ç. Yapar *et al.*, “Overview of the first pathloss radio map prediction challenge,” *IEEE Open Journal of Signal Processing*, vol. 5, pp. 948–963, 2024.
- [16] F.-H. Lin *et al.*, “Geo2ComMap: Deep learning-based MIMO throughput prediction using geographic data,” *IEEE Wireless Communications Letters*, vol. 14, no. 6, pp. 1831–1835, 2025.
- [17] X.-J. Li *et al.*, “RadioGAT: A joint model-based and data-driven framework for multi-band radiomap reconstruction via graph attention networks,” *IEEE Transactions on Wireless Communications*, vol. 23, no. 11, pp. 17777–17792, 2024.
- [18] Y. Zhou *et al.*, “TiRE-GAN: Task-incentivized generative learning for radiomap estimation,” *IEEE Wireless Communications Letters*, vol. 14, no. 5, pp. 1401–1405, 2025.
- [19] A. Banerjee *et al.*, “HORCRUX: Accurate cross band channel prediction,” in *Proc. 30th Annu. Int. Conf. Mobile Computing and Networking (ACM MobiCom)*, 2024, pp. 1–15.
- [20] Z. An *et al.*, “RadioTwin: A digital building material twin for wideband, cross-link, cross-band wireless channel prediction,” in *Proc. IEEE Int. Symp. Dynamic Spectrum Access Networks (DySPAN)*, 2025, pp. 1–10.
- [21] R. Chen *et al.*, “Transformer-based ray prediction for multi-band cellular handsets,” *arXiv preprint arXiv:2509.25722*, 2025. [Online]. Available: <https://arxiv.org/abs/2509.25722>
- [22] A. Alkhateeb, “DeepMIMO: A generic deep learning dataset for millimeter wave and massive MIMO applications,” 2019, dataset/Preprint. [Online]. Available: <https://arxiv.org/abs/1902.06435>
- [23] C. Yapar *et al.*, “Dataset of pathloss and toa radio maps with localization application,” 2022. [Online]. Available: <https://dx.doi.org/10.21227/0gtx-6v30>
- [24] S. Bakirtzis *et al.*, “Indoor radio map dataset,” 2024, accessed: Aug. 18, 2025. [Online]. Available: <https://dx.doi.org/10.21227/c0ec-cw74>
- [25] ITU-R, “Effects of building materials and structures on radiowave propagation above about 100 mhz,” International Telecommunication Union Radiocommunication Sector (ITU-R), Tech. Rep., Aug. 2023, recommendation ITU-R P.2040-3.
- [26] J. Hoydis *et al.*, “Sionna RT: Differentiable ray tracing for radio propagation modeling,” in *Proc. IEEE Globecom Workshops (GC Wkshps)*, Kuala Lumpur, Malaysia, 2023, pp. 317–321.
- [27] F. A. Aoudia *et al.*, “Sionna RT: Technical report,” *arXiv preprint arXiv:2504.21719*, 2025.
- [28] 3GPP, “Study on channel model for frequencies from 0.5 to 100 ghz (release 16),” 3rd Generation Partnership Project (3GPP), Technical Report 38.901, Dec. 2019.
- [29] C. M. Bishop, *Pattern Recognition and Machine Learning*. New York, NY, USA: Springer, 2006.
- [30] S. Mehta *et al.*, “Y-Net: Joint segmentation and classification for diagnosis of breast biopsy images,” in *Medical Image Computing and Computer Assisted Intervention – MICCAI 2018, Proc. Part II*. Berlin, Heidelberg: Springer, 2018, pp. 893–901.